



# A new approach of preheating and powder sintering in electron beam powder bed fusion

Jonas Böhm<sup>1</sup> · Christoph Breuning<sup>1</sup> · Matthias Markl<sup>1</sup> · Carolin Körner<sup>1</sup>

Received: 4 March 2024 / Accepted: 1 June 2024  
© The Author(s) 2024

## Abstract

Preheating is an essential process step in electron beam powder bed fusion. It has the purpose of establishing a sintered powder bed and maintaining an elevated temperature. The sintered powder bed reduces the risk of smoke and in combination with the elevated temperature improves the processability. Today, the line-ordering preheating scheme is widely used. This scheme does not take the previously built layers into account and results in an inhomogeneous elevated temperature and consequently in a variety of sinter degrees, which is disadvantageous for the process. The main challenge is now to modify this scheme to establish a homogeneous temperature distribution. This study addresses this challenge and analyses as well as optimises this scheme. A GPU-parallelised thermal model reveals a heterogeneous temperature distribution during preheating because of varying thermal conditions within a build job. In addition, a work-of-sintering model predicts that the sinter degree of the current powder layer on top of previously consolidated material is smaller than on top of the surrounding powder bed. This work aims to invert this trend to improve powder re-usage and material consolidation. Consequently, this work proposes an extension of the current scheme, compensating for the specific energy loss with local adjustments to the energy input. This adaptation results in a uniform temperature distribution and advantageous sintering. Applying the proposed numerical model proves to be an effective method to analyse the evolving process conditions and tailor the local energy input, thereby improving the efficiency of the preheating step.

**Keywords** Additive manufacturing · Electron beam powder bed fusion · Preheating · Numerical simulation · Macroscale · Optimisation

## 1 Introduction

Additive Manufacturing is well-known for its great potential in generating customised, complex components with the additional capability of achieving tailored local properties. For metallic components, powder bed fusion techniques in

particular enable the precise production of high-performance parts [1–4].

In contrast to the widespread use of lasers as an energy source, the electron beam exhibits several properties making it suitable for a number of applications. A key feature of powder bed fusion utilising the electron beam (PBF-EB) is the high power available, which can be up to 45 kW at current systems [5]. Combined with the possibility of deflecting the electron beam at very high velocities (up to 10,000 m/s), the electron beam can act as a general heat source, enabling process temperatures up to 1000 °C [6, 7]. This high-temperature environment facilitates the defect-free processing of crack-sensitive, non-weldable alloys, e.g. Ni-base superalloys, TiAl or refractory metals like tungsten and molybdenum [8–13]. Within laser-based powder bed fusion (PBF-LB), various approaches have emerged to benefit from the enhanced processability arising from elevated temperatures as well. A prevalent strategy is the employment of one or multiple additional lasers, which enables localised heating shortly before

---

✉ Jonas Böhm  
jonas.boehm@fau.de

Christoph Breuning  
christoph.breuning@fau.de

Matthias Markl  
matthias.markl@fau.de

Carolin Körner  
carolin.koerner@fau.de

<sup>1</sup> Chair of Materials Science and Engineering for Metals, Friedrich-Alexander-Universität Erlangen-Nürnberg, Martensstraße 5, Erlangen 91058, Germany

melting is performed. This offers opportunities to process even ceramic materials, reduce spatter and utilise a comparatively large-area pulsed laser for melting, consequently increasing total build rates [14–17].

In Contrast to PBF-LB, the heating step required to maintain high operating temperatures is inherent to the PBF-EB process itself. As sintering during this so-called preheating stage is mandatory to obtain a certain degree of stability in the powder bed. This is essential to prevent the repulsion of particles due to the charge imposed by incident electrons. Insufficient mechanical connection between the particles results in the explosive dispersion of the powder across the build platform, a phenomenon commonly characterised as smoke. Subsequently, an irregularly shaped powder bed emerges, causing complications in the accurate powder deposition and consolidation of succeeding layers. Furthermore, there exists a potential risk of powder particles being accelerated upon the beam column, leading to arc trips and, ultimately, fatal process failures [18].

Several strategies have been developed to address the smoke phenomenon. The machine manufacturer *Wayland Additive* eliminates the need for the preheating step by neutralising the evolving charge concentrations by a flow of oppositely charged particles [19]. An alternative approach involves a mechanical milling procedure prior to the process, manipulating the electrical properties of the powder particles' oxide layers [20–22]. These strategies allow for shorter cycle times, mitigate the risk of smoke formation and reduce the post-processing efforts, as the powder bed remains unsintered.

Another method, proposed by *Freemelt* to reduce the risk of smoke while maintaining high temperatures, involves the implementation of an intermediate heat source. This element, represented by either a graphite or refractory metal plate, is heated by the electron beam and subsequently transfers its energy to the powder bed through radiation. This configuration prevents any charge exposition of the powder bed. However, overall heating efficiency diminishes as heat radiation is not limited solely to the surface facing the powder bed [23]. Following a similar approach by facilitating photons instead of electrons Sjöström et al. integrated a Near-Infrared (NIR) heating device into the machine. Thereby, the suppression of smoke is unified with higher heating efficiency [24]. The primary drawback of these strategies lies in the need for additional machine equipment. Furthermore, the energy input of the proposed methods lacks the level of flexibility provided by the electron beam as heat source, which is characterised by its rapid and adaptable positioning.

This distinctive feature is an integral component of the standardised preheating strategy implemented in *GE Additive* machines. Within the established setup, the preheating step typically consists of two stages. In the first phase, designated as preheating one, the defocused beam repeatedly scans

the entire build area along a line-wise pattern. As preheating progresses, the powder bed is steadily gaining mechanical strength with ongoing sintering. This ensures that process-related beam deflections at very high speeds, often referred to as jumps, do not cause any smoke events. In the second stage, the preheating is concentrated around the future melt areas to enhance the sinter degree and temperature at these targeted positions [25–28]. Next to the positive influence of elevated temperatures on the processability, the augmentation of the sinter degree is also beneficial for the subsequent melting result. Specifically, it reduces the tendency of particle spattering and balling [29–33].

Based on the outlined preheating scheme, Drescher et al. systematically examined the impact of varying velocities during the second preheating stage to optimise layer times and therefore enhance the overall efficiency. Notably, a reduction in scanning velocity caused an exponential increase in compressive strength of the sintered powder bed. This led to the conclusion that efficiently accelerated sintering can be achieved through a more concentrated and localised heat input [27]. Lin et al. established a preheating window dependent on scan speed and beam spot size for NiTi powder, based on the pattern from stage one. The processing space itself faced constraints by either smoking of the powder or by a too excessive energy input resulting in partial melting of the powder. In accordance with the findings of Drescher et al., they demonstrated that a variation in the preheating velocity is possible even for alloys prone to smoke formation [34]. In another investigation addressing preheating, Shanbhag et al. formulated an empirically derived model linking the elevated temperature and the thermal conductivity of the powder bed. Thereby, they emphasised the critical role of the temperature level for the sinter result [28]. Despite these valuable contributions, the existing body of experimental work on the preheating stage remains relatively limited, presenting an opportunity for further investigations to deepen our knowledge of the thermal and sinter conditions during the process.

To gain a deeper understanding of what type of sintering is particularly happening during preheating, Yan et al. employed a thermal-fluid flow model for analysing liquid-state sintering and the phase-field method for depicting the solid-state sintering. Their study concluded that solid-state sintering is the predominant mechanism present during preheating, as typically only very small particles ( $< 20\mu\text{m}$ ) begin to liquefy. With the reduced number of those particles after repeated powder recycling steps, their importance for the sinter progress diminishes [35]. Rizza et al. also employed the phase-field method to correlate the neck growth during solid-state sintering of powder particles to the temperature profile from a build job measured at the base plate. The high spatial resolution and inclusion of multiple physical effects restricted the simulation to the modelling of two or

respectively three particles per simulation. As the main result of their studies, a model was established, capable of correlating the temperature history via the resulting neck radius to powder bed properties such as thermal conductivity. This information can serve as valuable input for accurate thermal simulations of the entire manufacturing process [36, 37]. For such extensive thermal simulations operating at full part scale, only a few efforts exist regarding PBF-EB. However, in terms of preheating the corresponding energy input is typically performed area-wise and averaged over the respective timespan, ignoring its inherent scan-wise nature [38, 39]. For the comprehensive modelling of the thermal history throughout an entire process this remains a valid method to realise the representation of the relatively large spatial and temporal domains. However, when shifting the focus on investigating and eventually optimising the preheating step, resolving the individual scan vectors becomes essential for accurately determining the temperature peaks.

This publication aims to assess the impact of the prevailing preheating scheme one on the distribution of the temperature and sinter degree of the powder bed. The motivation for this study arises from the examination of the thermal evolution during the preheating stage of a standard Ti-6Al-4V build job, as depicted in Fig. 1.

The conventional preheating pattern yields an inhomogeneous temperature distribution, primarily arising from the different thermal properties of the consolidated and powder sections. To systematically analyse this phenomenon with the ultimate goal of tailoring and improving the existing preheating procedure, a thermal model based on finite differences is deployed. The key feature of this model is its ability to represent the thermal evolution resulting from scan-wise preheating via the electron beam. In combination with a diffusion-motivated Arrhenius term, referred to as work-of-sintering, a direct relationship between the local temperature profile and the corresponding sinter progress is established [40, 41]. Utilising this correlation allows the presented approach to operate at a higher level of abstraction compared to existing simulations, considering the powder

as a continuum instead of individual particles and avoiding the need to explicitly resolve the diffusion of matter. This abstraction enables investigation of thermal and sinter conditions over complete preheating periods for representative build volumes, not being restricted to a limited number of individual powder particles [35–37]. In response to the sub-optimal result associated with the current way of preheating, we propose a novel optimisation-based strategy. This revised approach accommodates the observed differences by adjusting the preheating velocity locally.

## 2 Materials and methods

### 2.1 Experimental

The PBF-EB process, serving as a benchmark for the numerical model, was performed on a freely programmable machine developed by *pro-beam AG & CO. KGaA (Gilching, Germany)*. It is equipped with a 15 kW electron gun operating at a high voltage of 150 kV. The experimental setup mimics a standard build job, which has been carried out similarly numerous times, especially for material development purposes. As model material serves Ti-6Al-4V from *Tekna Advanced Materials Inc.* with a particle size distribution between 45  $\mu\text{m}$  and 105  $\mu\text{m}$ , an apparent density of 2.49  $\text{g}/\text{cm}^3$  and a tap density of 2.8  $\text{g}/\text{cm}^3$ . The choice of the material is of minor importance as the temperature variations result from differing thermal properties between powder and consolidated material. The nine molten components share a simple cuboid shape with a base area of 15 mm x 15 mm and the spacing between neighbouring specimens is 7.5 mm. Connection to the steel base plate, which exhibits the dimensions of 185 mm x 185 mm x 30 mm, was provided by cylindrical supports, each 3 mm in height.

The regular PBF-EB routine of lowering the platform, applying a new layer of powder, preheating, melting and electron optical (ELO) imaging was deployed. Each of the nine samples was molten according to the snake strategy

**Fig. 1** Snapshots of the preheating procedure of a Ti-6Al-4V build job manufacturing nine cuboid specimens deploying a line-ordering scheme [25]. (a) After applying a new powder layer. (b) After 4.5 s of preheating. (c) After 17 s of preheating

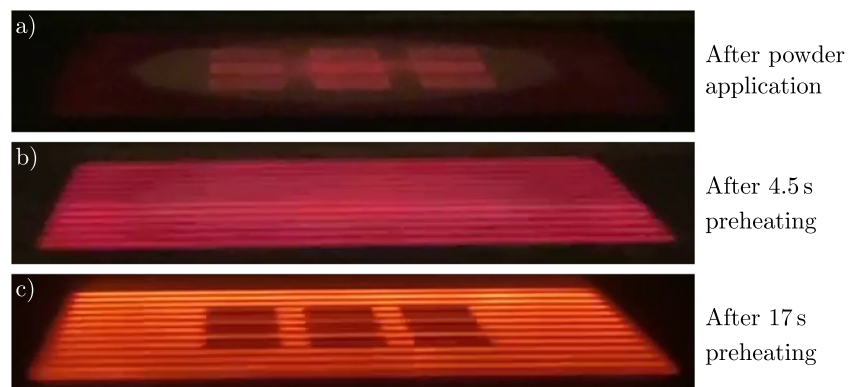
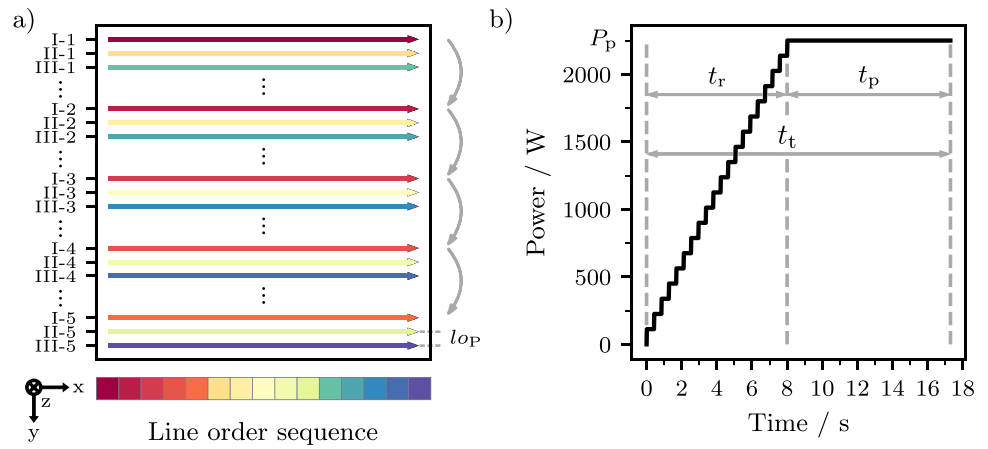


**Fig. 2** Preheating procedure. (a) Schematic of the line-ordering pattern. (b) Power during the progress of the preheating stage, exhibiting a ramp followed by a plateau phase



with identical parameter values. The power applied during hatching  $P_H$  was set to 800 W, the offset between two adjacent lines  $lo_H$  to 100  $\mu\text{m}$  and the hatch velocity  $v_H$  to 8 m/s. An empirically determined pause of approximately 6 s was implemented between powder raking and the onset of preheating to promote the formation of connections with the preceding layer. Throughout the entire process, the temperatures at the base plate  $T_{\text{base}}$  and at the surrounding heat shield  $T_0$  were recorded via K-type thermocouples. The process log files additionally include the time-resolved power and focus values.

In contrast to the melting phase, the beam operates in a defocused state during the preheating stage. This adjustment ensures a more uniformly distributed energy input and a reduction in the local energy density, avoiding unintentional powder melting. The applied standard preheating scheme follows the recommendations from Larsson and Snis [25]. According to their patent, the building area is systematically scanned along straight parallel lines, covering an area denoted as  $A_p$ . To prevent smoke events, a designated time must elapse before the beam returns to a prior spot. For a defined area, this time interval is mainly governed by the selected preheating velocity  $v_p$  and the respective line offset  $lo_p$ . Additionally, consecutive paths must be sufficiently separated to avoid interference with the effects caused by the previous pass of the electron beam. Thus, a line-ordering strategy is implemented, where every  $n$ -th line is scanned and the starting index shifts by one with each repetition until the entire pattern is completed (see Fig. 2a). How often the aforementioned pattern is repeated, is determined by the total preheating time  $t_t$ , which is the sum of the duration of the ramp  $t_r$  and the plateau stage  $t_p$ . These terms are linked to the modulation of power during the preheating period, as displayed in Fig. 2b. Initially, the power starts at zero and increases incrementally until a defined plateau  $P_p$  is reached, with the number of ramp steps denoted as  $s$ . The specific values used in the experiment are outlined in Table 1.

## 2.2 Simulation

### 2.2.1 Physics

For the computation of temperatures  $T$  during the preheating stage, a thermal model is employed based on the heat conduction equation

$$\frac{\partial T}{\partial t} = \nabla \cdot (\alpha \cdot \nabla T), \tag{1}$$

where time is denoted by  $t$ . Different thermal diffusivities  $\alpha$  of powder  $\alpha_p$  and consolidated material  $\alpha_c$  are applied.

The heat flux generated by the electron beam  $\dot{Q}_b$  is modelled as surface heat source

$$\dot{Q}_b(x, y, t) = \eta \cdot P(t) \cdot I(x, y), \tag{2}$$

expressed as the product of the applied power  $P$  and the electron absorption coefficient of the material  $\eta$  along a normed 2d-intensity distribution  $I$ , where  $x$  and  $y$  define the respective spatial position.

**Table 1** Preheating parameters

Property	Symbol	Value	Unit
Preheating area	$A_p$	125 x 125	mm <sup>2</sup>
Preheating velocity	$v_p$	16.6	m/s
Preheating line offset	$lo_p$	1	mm
Line order	$n$	10	–
Total preheating time	$t_t$	17.3	s
Ramp time	$t_r$	8	s
Plateau time	$t_p$	9.3	s
Number of ramp steps	$s$	19	–
Preheating plateau power	$P_p$	2250	W
Focus current	$I_p$	3000	mA

Assuming a regular Gaussian distribution for the beam profile would be insufficient due to the changed intensity distribution of the defocused electron beam during the preheating stage. Consequently, a pinhole measurement was performed with the identical beam settings of the experimental preheating phase, as described in Section 2.1. The obtained measurements were fitted with a super-Gaussian profile  $\tilde{I}$  (see Fig. 3), which is subsequently integrated as a normalised approximation of the beam shape

$$\tilde{I}(x, y) = \exp \left[ - \left( \left( \frac{(x - x_b)^2}{2\sigma_x^2} \right)^{p_x} + \left( \frac{(y - y_b)^2}{2\sigma_y^2} \right)^{p_y} \right)^p \right], \tag{3}$$

$$I(x, y) = \tilde{I}(x, y) \left( \int_0^{y_{max}} \int_0^{x_{max}} \tilde{I}(\tilde{x}, \tilde{y}) \, d\tilde{x} d\tilde{y} \right)^{-1}. \tag{4}$$

The  $\sigma$ -values in the specific direction correspond to  $\frac{1}{4}$  of the beam diameter in case of a regular Gaussian distribution. The exponents  $p_x$ ,  $p_y$  and  $p$  serve as fitting parameters to account for the super-Gaussian shape of the defocused beam, the specific values are provided in Table 2 in the Appendix. The beam centre is denoted as  $(x_b, y_b)$  and the spatial domain ranges from 0 to  $x_{max}$  and  $y_{max}$ .

Given that the heating process contributes significantly to the overall layer time, it becomes essential to include effects such as heat radiation within the model, which may be negligible when only considering short durations, e.g. during the melting process [42]. The radiative heat flux  $\dot{Q}_{rad}$  is modelled according to the Stefan-Boltzmann law

$$\dot{Q}_{rad} = \epsilon \cdot \sigma_{SB} \cdot A \cdot (T^4 - T_0^4), \tag{5}$$

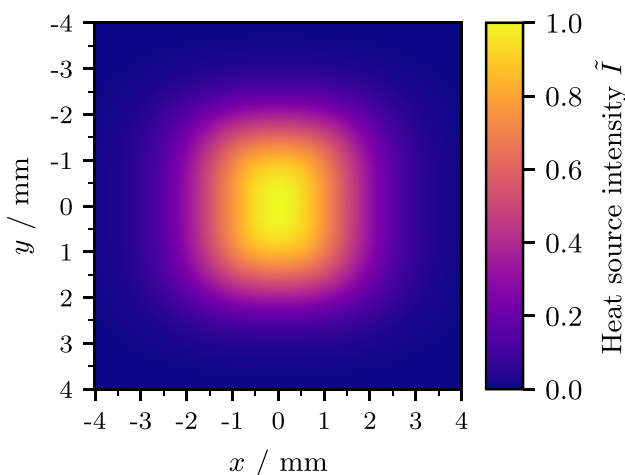


Fig. 3 Schematics of the non-normalised super-Gaussian beam profile

where  $T_0$  denotes the surrounding temperature, measured at the heat shield. The emissivity of the surface material is represented by  $\epsilon$ , the corresponding area by  $A$  and the Stefan-Boltzmann constant is denoted by  $\sigma_{SB}$ .

Convection is regarded as negligible due to the vacuum environment. Furthermore, with the absence of melting during preheating, neither evaporation nor latent heat are included. The material properties for Ti-6Al-4V are set constant and are primarily taken from Milošević and Aleksić for a reference temperature around 1000 K [43], which is frequently deployed as target preheat temperature for this material. Detailed values for these properties are provided with the relevant constants in Table 3 in Appendix. Furthermore, the thermal diffusivity of the powder continuum is assumed to be one order of magnitude lower than that of the bulk material according to the investigations of Smith et al. [44], with changes during preheating being excluded from the model. Averaging of the differing properties between powder and bulk material is done via the arithmetic mean according to the investigations of Kadioglu et al. [45].

To obtain a quantitative measure of the sinter behaviour during preheating, the established concept of the work-of-sintering  $\phi$  [40, 41]

$$\phi(t, T(t)) = \int_0^t \frac{1}{T(\tilde{t})} \cdot \exp \left( - \frac{Q}{RT(\tilde{t})} \right) d\tilde{t} \tag{6}$$

is employed.  $Q$  represents the activation energy for sintering and  $R$  the universal gas constant. The driving force for sintering is the reduction of free surface energy. Due to the high surface-to-volume ratio, this is naturally high for powders. The limiting factors of the sinter process are the kinetics, governed by different diffusion processes. The formulation of the work-of-sintering is centred around the Arrhenius term, which emphasises the diffusion-controlled character of sintering. By applying such a representative value, the objective is not to precisely quantify the sinter degree or determine the densities of the powder bed. Instead, its purpose is to facilitate a quantitative comparison of the effects that specific strategies have on the sinter behaviour. Due to the exponential dependence of  $\phi$  on  $T$ , it is essential to explicitly resolve the individual scan tracks in the model.

### 2.2.2 Numerics

To solve the differential heat conduction equation, an explicit finite difference (FD) scheme is applied by employing the forward time-centred space (FTCS) approach [46]. The computational operations are optimised for the use of a graphical processing unit (GPU) and run on a Nvidia A100 provided by the high-performance computing environment at FAU. Operating on a three-dimensional grid (see Fig. 4), the model features an equidistant discretisation  $dx = dy$  in the x-y



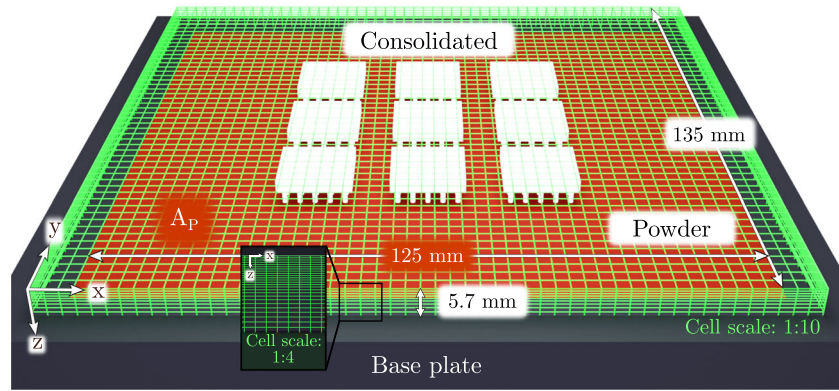


**Fig. 4** Schematics of the simulation setup approximating the experimental design of the reference process. The discretisation of the simulation domain is represented by the green mesh at a resolution scale of 1:10, while the cuboid specimens are displayed in white and

the residual cells are filled with powder (not shown). The mesh coarsening is displayed in the separate window with a resolution scale of 1:4. The size of the preheating pattern is marked in red and the base plate in grey

plane and a coarsened mesh in  $z$ -direction. This enables the depiction of larger volumes, especially as the solution of the heat conduction equation becomes increasingly linear with extended distance to the energy source. Therefore, the first  $k$  planes of cells towards the depth maintain a comparatively fine discretisation of  $dz_s$  and after this coarsening index  $k$ , the size of cells in  $z$ -direction linearly increases towards the final cell size of  $dz_e$ . The domain covers the square area of the preheated powder bed plus a spacing of 5 mm in each lateral direction, with a depth  $l_z$  of 5.7 mm, totalling approx. 25 million cells. For the specific input values of the simulation the reader is referred to Table 2 in the [Appendix](#).

Regarding the boundaries of the system, different thermal conditions are incorporated. At the top of the domain, the heat input is determined by the electron beam according to Eq. 2 and the respective heat loss is governed by the radiative heat flux described in Eq. 5. The surrounding temperature  $T_0$  determining the radiative heat flux is set constant, as the logged values stay within a temperature interval of 1 °C during the considered preheating step. The conversion of the heat flux to the corresponding temperature change per time is calculated according to the cell dimensions, the specific heat capacity  $c_p$  and the density  $\rho$ . For the powder cells a packing density  $\rho_{pac}$  of 50% is assumed. A Dirichlet boundary is imposed at the bottom, as the experimentally measured temperature at the base plate  $T_{base}$  is almost constant, varying also 1 °C during the preheating step. On the remaining edges, the choice of the boundary condition is of reduced significance as the characteristic thermal length  $l_{th}$  calculates to approximately 3.1 mm for the total preheating time, while the additional spacing in the specific directions is 5 mm. In the current implementation, the temperature gradient in the out-flow direction is adapted from the preceding cell to maintain a constant heat flux in this direction.

In terms of temporal discretisation, it was ensured that the timestep  $dt$  satisfies Neumann's stability criterion for three-dimensional FTCS schemes [47]

$$dt_{max} \leq \frac{dz_s^2}{6\alpha_c}. \quad (7)$$

Considering the two different  $\alpha$ -values and the non-uniform spatial grid, the maximum thermal diffusivity  $\alpha_c$  and the minimum grid spacing  $dz_s$  are used to estimate the maximum possible timestep  $dt_{max}$  of approximately  $7.3 \times 10^{-5}$  s. To enable a precise energy input, the heat flux from the electron beam is derived through subsampling of the point heat source. During the selected timestep  $dt$  the beam centre passes three cells when moving with  $v_p$ . In contrast, the subsampling process operates at a smaller timestep  $dt_{sub}$ , equivalent to 33% of  $dt$  and therefore covering each cell. Following the subsampling sequence, the conduction step is computed for every  $dt$ .

The initial temperature distribution at the start of the preheating step is a result of simulating the processing of the previous five layers. All relevant process steps (melting, ELO-imaging etc.) are modelled according to the assumptions of the present model. The exact times, focus and power values are adapted from the process log files of the build job described in Section 2.1. The application of a new powder layer is represented by adding the respective number of powder cells atop the domain, each with an initial temperature  $T_{i,p}$ . The temperature variations between layers diminish with an increasing number of layers, approaching a quasi-steady state. In this state, temperature distributions are shifted only by the corresponding effective layer thickness  $d_l$ .

### 3 Results and discussion

In the forthcoming section, the thermal evolution during the standard preheating stage is presented including a qualitative comparison between numerical and experimental results. Subsequently, conclusions about the sinter behaviour are drawn, as the work-of-sintering is evaluated throughout the simulation of the preheating stage. Based on the findings of this section, an adaption to the preheating strategy is proposed, accounting for the different thermal properties of the heterogeneous volume.

#### 3.1 Standard preheating

##### 3.1.1 Temperature evolution

On the left side of Fig. 5 four representative snapshots of the preheating process are displayed and compared with the corresponding numerical results on the right.

In the initial situation at  $t = 0.0$  s (Fig. 5a), the newly raked powder exhibits the highest temperature values above the previously molten samples. This aligns with the temperature distributions after melting. While the molten samples experienced intense heat input during the melting stage, the surrounding powder primarily cooled down mainly due to heat radiation. As the preheating stage progresses, the thermal situation of the top powder layer begins to assimilate (Fig. 5c). The temperature of the particles above the samples decreases while the surrounding powder increases its energy content. This development arises from the higher thermal conductivity of consolidated matter compared to powder. The more efficient heat dissipation leads to a decline in temperature at the corresponding sites on top, while conversely, in regions with powder underneath the energy accumulates near the surface. This trend continues until the end of the preheating phase, as shown in Fig. 5g, resulting in a visible difference between high temperatures above powder and low temperatures upon consolidated material.

Given the drop in temperature at the areas with consolidated matter underneath, the only way to reach a specific temperature level at the intended melt zones is a significant increase in power, when applying the standard strategy. This, in turn, results in the powder regions experiencing an even more pronounced overheating.

The elevated temperatures appearing above powder can be critical during the process. With increasing temperatures, the layers expand, begin to sinter and gain mechanical strength by forming inter-particle connections. Once the preheating phase has elapsed, the regions not designated for melting cool down, leading to contraction and thereby to mechanical stresses. In combination with the mechanically comparatively unstable sintered powder, the probability of forming cracks in the powder bed also increases.

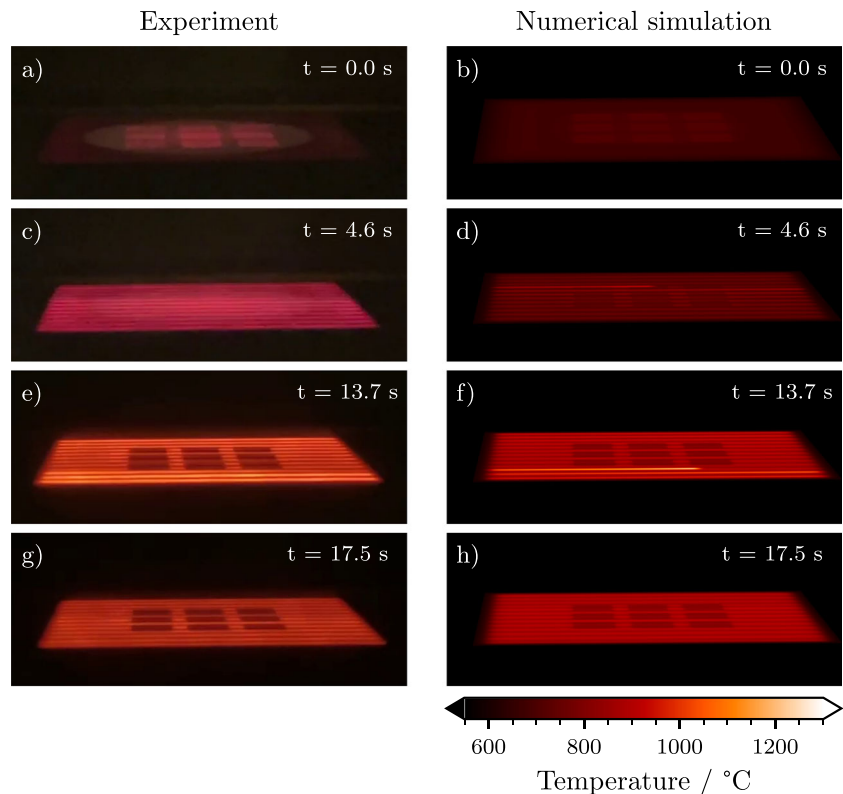
A further examination of the resulting temperature profile reveals that the line-wise scanning of the electron beam over the surface induces local variations. This inhomogeneous energy input is necessary to provide sufficient return times. Nevertheless, these local differences dissipate within a few seconds after preheating and do not represent a major problem for subsequent processing. A critical threshold is only surpassed when the local energy input exceeds a specific limit, leading to unintentional powder melting.

On the right side of Fig. 5, the corresponding numerical results are presented. The comparison between the experimental and numerical results is performed qualitatively. The simulation additionally provides a quantification of the temperature, depicted by the *matplotlib* colourmap *gist\_heat*, which emulates the blackbody radiation from a metal bar as it increases its temperature [48].

Upon the detailed comparison at four representative timesteps, it becomes apparent that the simulation results generally align well with the experimental observations. The temperature distributions between the two distinct regions at the surface are accurately depicted, showing the opposite temperature evolutions of the powder areas above consolidated and powder material as preheating progresses.

However, in reality, the point in time, when both regions exhibit a similar temperature, is delayed by approximately 1.5 s compared to the numerical simulation. This minor misalignment is believed to arise from a too-low initial temperature at Fig. 5b, as indicated by the comparison with the experimental reference in Fig. 5a. The reason for this discrepancy may be excessive energy losses during melting prior to the preheating phase. The applied radiation model assumes the relatively low temperature of 250 °C as the surrounding temperature for the melting stage as well. The temperature measurement at the heat shield is not sensitive to short temperature rises at the build plane. Therefore, by utilising this value, energy losses during brief temperature peaks are overestimated, while the general surrounding temperature during the longer preheating should be correctly represented. Considering the total duration of the preheating time (17.3 s), the identified inaccuracy of approximate 1.5 s deviation appears as an acceptable error and could be improved by refining the measurement of the surrounding temperature. By comparing the intermediate timesteps in Fig. 5c and e with the numerical results in Fig. 5d and f, it can be observed that the line-shaped temperature elevations resulting from the previous beam pass appear more defined and pronounced in the simulation. Regarding these observations, it has to be considered that the optical images are captured through a lead glass and a fine grid. Those are positioned behind the viewport to prevent exposure to x-ray radiation and metallisation of the window. In combination with the rough powder surface, this leads to a more diffuse impression of the situation compared to the rendered picture of the simulated continuum. Additionally, the colourmap is

**Fig. 5** Qualitative comparison between images captured through the observation window of the machine (**a, c, e, g**) and the thermal numerical simulation (**b, d, f, h**) for four representative timesteps of the preheating stage. The colourbar for the numerical results emulates the blackbody radiation from a metal bar as it increases its temperature



chosen to mimic the incandescence, but in order to draw precise conclusions about the actual temperature distribution, quantitative measurements have to be performed. This is also supported by the fact that the colour displayed in the snapshot in 5c is not represented by the *gist heat* map at all.

Nevertheless, the depiction of the diverse thermal developments enables the simulation to make valid predictions about the emerging thermal situations during preheating. Moreover, considering that one minute of computational time equals one second of real-time, the proposed model appears appropriate for studying the effects and developments of the preheating phase in a reasonable timeframe.

### 3.1.2 Sintering

Apart from ensuring the proper tempering of the powder bed, the primary objective in integrating the preheating step into the process cycle was to establish a mechanically stable connection among the powder particles. In Fig. 6 the numerically obtained temperature (a) as well as the corresponding work-of-sintering (b) distribution are represented at the end of the preheating stage.

It becomes apparent, that the change in work-of-sintering aligns with the non-uniform temperature distribution. The sinter behaviour itself is governed by the individual temperature peaks, as it can be observed in Fig. 6c for an exemplary location above powder and in Fig. 6d above consolidated

material. Since the temperature values are a superposition of the dissimilar prevailing temperatures and the rise resulting from the direct energy input of the beam, the peaks and subsequently the sintering rate differ also accordingly.

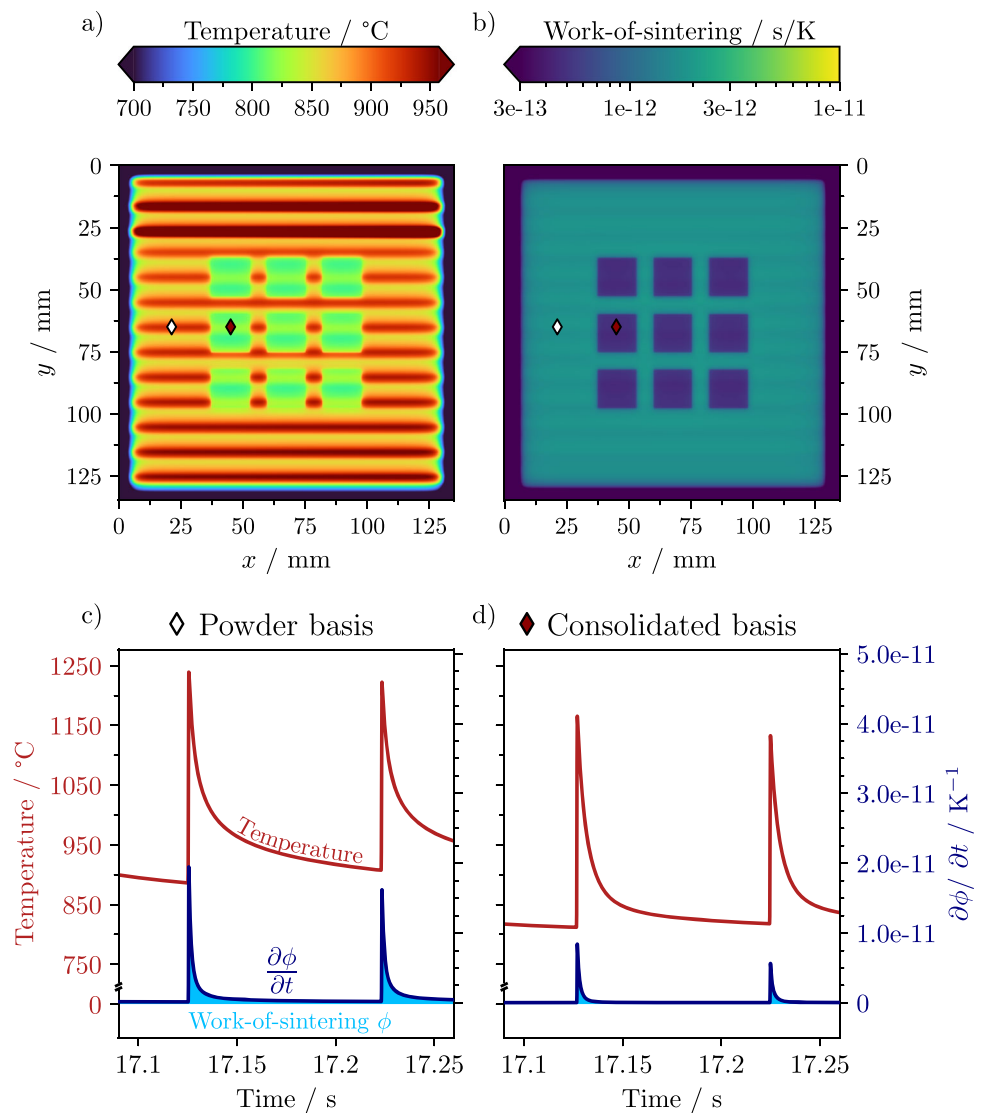
The discrepancy in the work-of-sintering along the preheating area highlights the inefficiency of the standard preheating strategy. While achieving a minimum required sinter degree at the designated melt surfaces, the connection between the particles at the residual regions rises rapidly, providing no process-related benefits but instead hindering the subsequent powder removal. For improved process efficiency, it would be advantageous if the sinter progress was distributed inversely, with the highest values at locations where the actual melting will occur. The enhanced connection among particles at these positions would mitigate the risk of balling as well as the tendency for particle spattering [29–33].

### 3.2 Tailored preheating

After identifying the shortcomings of the standard preheating approach, the subsequent section aims to propose a more tailored strategy in alignment with the requirements of the actual process. Preheating should ensure a high level of temperature at future melt sites while preventing the overheating of the residual powder. Regarding the sinter result, a general principle can be formulated — areas not subsequently molten



**Fig. 6** Numerically obtained spatial temperature (a) and work-of-sintering field (b) at the end of the preheating stage. The local evolution of the temperature and the work-of-sintering rate is displayed for representative positions with powder (c) and consolidated matter (d) underneath



should be sintered as intensely as necessary and as slightly as possible, while the opposite is valid for respective melt regions, as described in Section 3.1.2. Furthermore, in most cases, the degree of sintering is also the critical factor determining the required preheating time, significantly impacting the total build time and thereby, the efficiency of the entire build process.

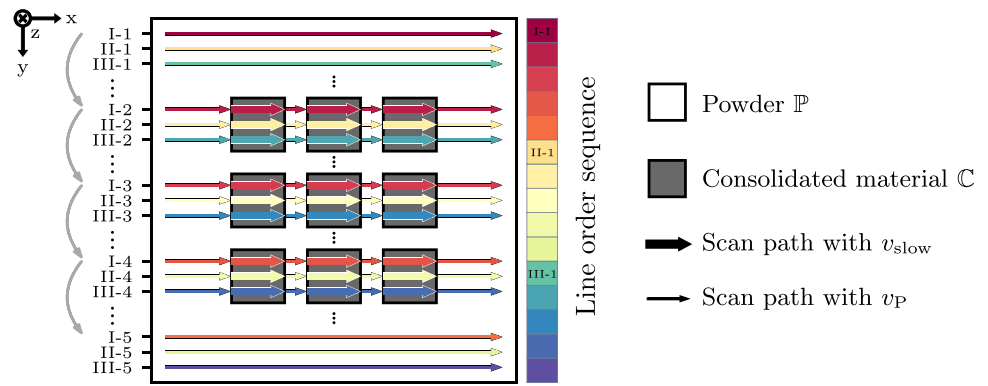
In the present work, we follow the objective of achieving a uniform temperature distribution to prevent the overheating of powder areas. Consequently, we will systematically examine the impact on the corresponding sinter result. As outlined in Section 3.1, the origin of the heterogeneous temperature distribution lies in the dissimilar thermal conductivities of the underlying matter. This can only be compensated by a local adjustment of the energy input. The heat input is governed by the electron beam, characterised by its shape, power and deflection velocity. When scanning along a straight line over a melt surface with a length of 15 mm at a set velocity

of 16.6 m/s, the total residence time above the corresponding area remains below 1 ms. Within 1 ms neither the shape of the beam nor the power can be effectively manipulated. These parameters typically require several tenths of a second to reach their corresponding target value.

In contrast, the inertia-free electromagnetic deflection system of PBF-EB machines enables the sufficiently fast adaptation of the velocity. So, the proposed approach is based on locally modifying the velocity to compensate for the different energy losses with an adapted energy input. Therefore, the standard velocity is reduced to  $v_{slow}$  above regions with more efficient heat conduction towards the bottom, extending the residence time of the energy source at these specific positions. A schematic representation of the strategy is illustrated in Fig. 7.

This approach faces as limitation that the velocity cannot be altered without constraints. The upper boundary is determined by the local return time, critical for managing

**Fig. 7** Graphical illustration of the adapted preheating scheme. The width of the arrows corresponds to the velocity of the individual scan track with thicker lines indicating slower velocities and, consequently, higher energy inputs



the risk of smoking, while the lower boundary is governed by the potential unintended melting of particles. In order to conduct a thorough comparison between the standard and locally adapted preheating scheme, all parameters (pattern, power, time, etc.) remain constant, except for the local velocity and consequently the number of repetitions of the entire pattern. Even if the current exemplary structures exhibit a relatively simple shape, the usual applications of PBF-EB include complex, three-dimensional geometries, which complicate precise analytical predictions of the corresponding velocity values.

The combination of a numerical model with an optimisation algorithm offers the distinct advantage of automatically determining more suitable velocity values. The optimisation problem is generally designed to minimise the discrepancy in the median temperatures of the different regions in the preheating area. In this particular scenario, involving only two separate regions, the velocity adaption was limited to the areas requiring higher energy input. The objective function  $\xi$  is described by

$$\xi(v_{\text{slow}}) = \sum_{t=t_f}^{t_i} \left( \text{median}_{(x,y) \in \mathbb{P}} (T(v_{\text{slow}}, t, x, y)) - \text{median}_{(x,y) \in \mathbb{C}} (T(v_{\text{slow}}, t, x, y)) \right)^2, \tag{8}$$

where  $\mathbb{P}$  and  $\mathbb{C}$  represent the sets of preheating coordinates with powder or respectively consolidated matter underneath. The median of the temperature along the corresponding regions is utilised for valid determination of the general temperature level at each section so that the influence of local temperature peaks is not overestimated. The objective function is assessed every  $n$ -th timestep and the summation of the results begins after the power ramp and covers the residual total preheating time. The iteration interval  $n$  was set to 5000, a sufficiently substantial lot size for the evaluation.

Given the absence of a closed-form solution for the problem, a black-box optimisation algorithm was employed. Considering the computationally expensive nature of a single function evaluation, a Bayesian optimisation scheme,

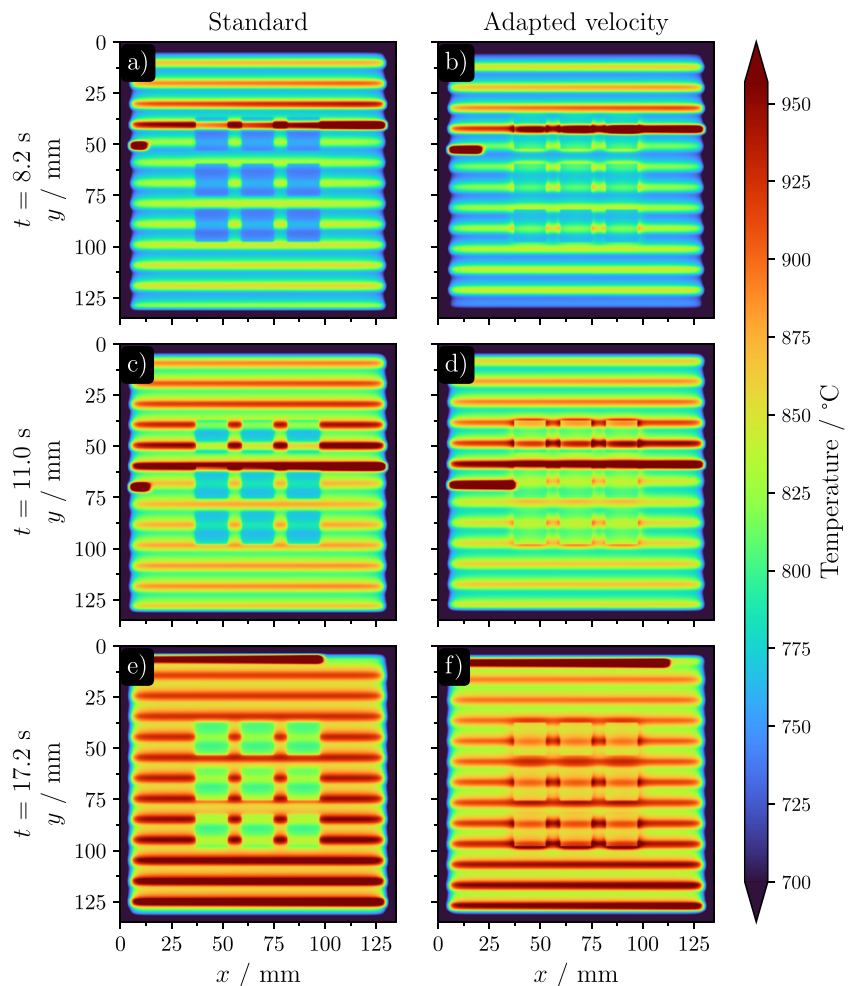
implemented in the scikit-optimize library [49], seemed to be well-suited. Interested readers can find a comprehensive description of this standard algorithm in multiple works within the existing literature [50–52].

The final values of the velocities are  $v_{\text{slow}} = 9.1$  m/s for the areas above consolidated and the previously employed  $v_p = 16.6$  m/s above powder material. By lowering the velocity above consolidated matter smoke is effectively prevented, as the local return time is further extended while still remaining sufficient with respect to the lower melting limit. The temperature peaks do not exceed the decisive liquidus temperature.

In Fig. 8 the temperature evolutions for the standard and the adapted preheating scheme are compared. In contrast to the non-uniform temperature distribution discussed in-depth in Section 3.1, the energy-compensating approach successfully achieves an almost homogeneous temperature profile between the two identified different regions. As the total energy input remains constant with the current setting, the prevailing temperature above powder decreases slightly, but the temperature at regions with consolidated matter underneath assimilates. The temperature rise at these sites indicates that reaching a minimum temperature at each position in the preheating area requires less power or time compared to the previous strategy. This contributes to a more efficient utilisation of available resources regarding the thermal evolution.

Figure 9 shows a comparative analysis of the two preheating strategies in regard to the sinter behaviour. Figure 9a displays the spatial distribution of the work-of-sintering at the end of the preheating period. Focusing on the upcoming melt areas, the altered strategy achieves a work-of-sintering more than one order of magnitude higher than the standard scheme. This is attributed to the higher local energy input resulting from the reduced velocity, leading to elevated prevailing and peak temperatures. These temperature maxima contribute disproportionately to the work-of-sintering, according to the exponential nature of the relationship denoted in Eq. 6. The residual area, designated for removal after the build process, displays a lower work-of-sintering nearly everywhere compared to the standard pattern. This results in reduced powder

**Fig. 8** Comparison of the numerically obtained temperature profiles of the standard (left) and the adapted preheating strategy (right) for three representative timesteps

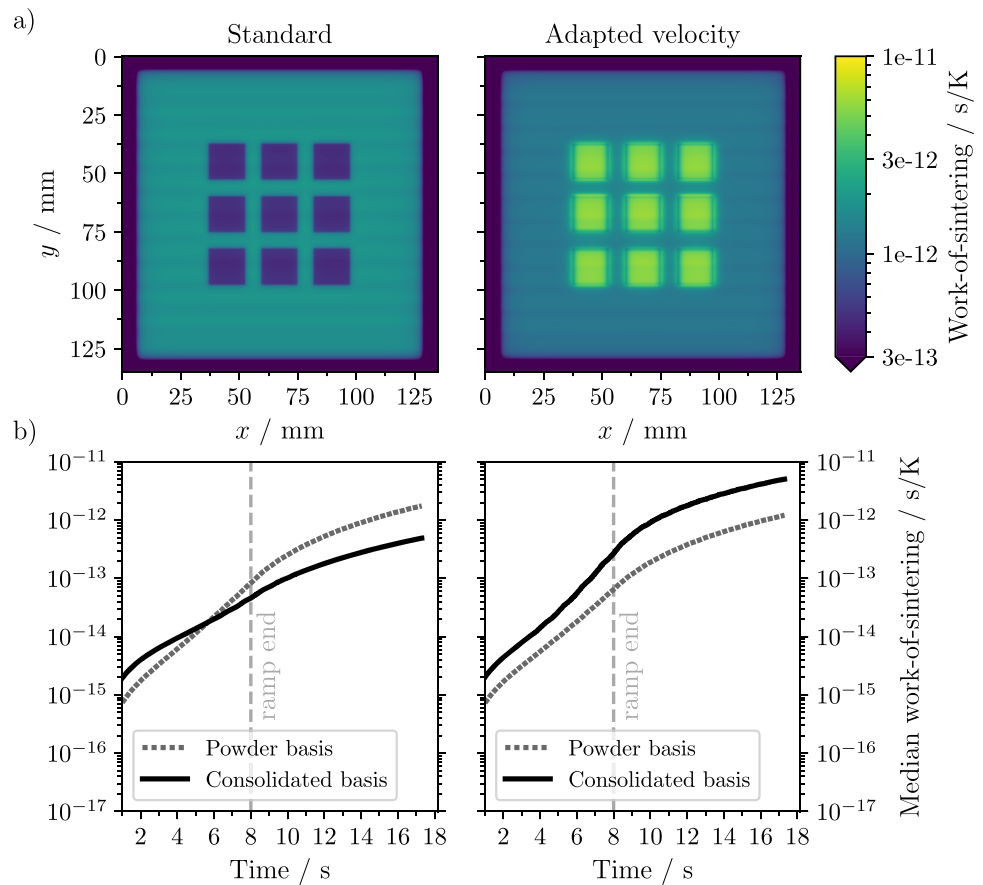


recycling efforts. Notably, the work-of-sintering remains approximately twice as high as for powder at the melt surfaces following the standard strategy. Only the small regions directly adjacent to the zones with reduced velocity experience a different situation. Due to the relatively large beam diameter deployed in the preheating stage, the representation of sharp edges becomes considerably inaccurate. As a result of this inaccuracy, these distinct areas also experience an increased energy input due to the slower beam movement, leading to elevated temperatures and sinter degrees compared to the residual powder regions. The most effective countermeasure for this effect would be the reduction of the beam diameter, providing a higher resolution in depicting geometries.

Given the same resources of time and power, the new strategy demonstrated an improved sinter outcome at the sites designated for melting, accompanied by a reduced connection in the majority of areas intended for subsequent removal. It can therefore be concluded that the sinter result of the individual regions is well-tailored to the respective purpose.

To further assess the efficiency of the individual strategies it is important to gain a comprehensive understanding of the temporal evolution of the work-of-sintering. Consequently, Fig. 9b depicts the sinter progress for the different regions during the preheating stage. When comparing the overall trends, they show similar behaviour, differing mainly in the magnitude of the individual slopes. Equation 6 indicates that a constant temperature leads to linear progress as time advances, presented as a logarithmic relationship with the selected semi-logarithmic scale in the displayed plot. This situation can be observed in the late stage of preheating when the  $T^4$  dependency of radiative losses limits the achievable temperature for a specific energy input. The differing behaviour at the beginning can be explained by the relatively sharp rise in temperature during the initial stage of preheating, where the radiation still has a minor impact. Furthermore, the kink occurs shortly after the completion of the power ramp. The transition towards the linear relationship between time and work-of-sintering indicates that once the maximum power is applied the temperature rapidly reaches

**Fig. 9** Work-of-sintering results of the standard (left) and the adapted strategy (right). **(a)** Display of the work-of-sintering distribution at the end of the preheating stage. Mind the distinct absolute differences, which require a logarithmic scale. **(b)** Temporal evolution of the median work-of-sintering value for powder above powder and consolidated matter



its quasi-steady state, marking the stage with the most substantial sinter progress.

The results of the standard preheating scheme (left) reveal that, initially, the powder above consolidated matter shows higher values than the residual powder. This is attributed to the transfer of residual heat from the preceding melting process. As preheating advances, in accordance with the opposing thermal development illustrated in Fig. 5, particles above powder volumes begin to experience a persistent, higher work-of-sintering. The divergence of the work-of-sintering starting at approximately 6 s creates a sintering distribution opposite to the requirements of the melting process. This development is intensified with proceeding time. In contrast, for the adapted strategy (right), no intersection of the work-of-sintering occurs, and the powder above consolidated matter consistently displays higher values. Despite maintaining nearly constant temperatures across the regions, the respective melt sites start at an elevated temperature and exhibit more intense temperature peaks due to the reduced local velocity, explaining the observed sinter outcome.

In the present case, the proposed concept of tailoring the local energy input is simplified with a basic example involving only two regions with differing thermal properties. However, the transfer of this method to more complex geometries featuring multiple thermal situations should follow the

same principle. Thereby, each region is assigned an individual velocity based on the extent of the local heat loss and the initial thermal conditions. Utilising the numerical simulation facilitates the resource-saving determination of the required energy input and consequently, the corresponding velocity to achieve the desired objective.

Possible objectives of the preheating phase range from dissipating excess energy at sites with prior high-energy input to enhancing the sinter degree in powder regions, enabling processing without support structures. The variety of different geometries and materials can bring numerous challenges along. Thus, the presented example is not intended to serve as the universally valid way of how preheating has to be performed. Instead, it aims to show the capabilities that a customised energy input can provide. Furthermore, it should highlight the significance of the preheating step as well as the available optimisation potential for this process stage using the efficient means of numerical simulation.

## 4 Summary and conclusions

This study aimed to evaluate and optimise the commonly employed line-ordered preheating strategy. In order to depict the thermal conditions during the preheating stage of



PBF-EB, a GPU-parallelised numerical model was introduced and qualitatively validated. The model was extended with a temperature history-dependent measure of the sinter degree, enabling conclusions about the efficiency of the preheating strategy.

Results from the standard preheating scheme reveal an inhomogeneous temperature distribution and a suboptimal sinter outcome. Due to the different thermal diffusivities of consolidated and powder material, more heat is conducted towards the base plate by the consolidated matter. Consequently, this results in lower temperatures and less intense sintering in the powder layer above these regions. The newly proposed strategy locally adapts the energy input by selectively adjusting the velocity to compensate for the non-uniform energy loss. This approach successfully achieves a homogeneous temperature distribution and aligns the sinter degree with the requirements of the presented example, exhibiting the highest work-of-sintering at the designated melt areas and less sinter progress at the regions intended for subsequent removal.

In general, the proposed numerical model effectively provides insights into the thermal and sinter evolution during preheating. Through the identification and analysis of prevailing conditions, it can assist in determining the appropriate values for implementing the tailored strategy. As the next step, systematic experimental verification is planned combined with an extension of the approach to multiple materials and different geometries with a special focus on the time-saving potential of the approach. To further exploit the residual optimisation potential of the preheating stage, a more comprehensive understanding of individual influencing factors such as beam diameter, line offset, power, etc. would be essential. In the current study, only the velocity was subject to change, while multiple other parameters remained constant. In the future, this gap will be filled by employing a systematic high-throughput approach.

### Appendix

**Table 2** Simulation input data

Property	Symbol	Value	Unit
Super-Gaussian parameters	$\sigma_x$	1.32	mm
	$\sigma_y$	1.39	mm
	$p$	0.79	–
	$p_x$	1.28	–
	$p_y$	1.68	–
Grid spacing in x and y direction	$dx = dy$	250	$m \times 10^{-6}$
Coarsening index	$k$	53	–
Initial grid spacing in z-direction	$dz_s$	50	$m \times 10^{-6}$
Final grid spacing in z-direction	$dz_e$	125	$m \times 10^{-6}$
Temperature at heat shield	$T_0$	250	°C
Temperature at base plate	$T_{base}$	709	°C
Initial powder temperature	$T_{i-p}$	150	°C
Regular timestep	$dt$	$4.5 \times 10^{-5}$	s
Subsampling timestep	$dt_{sub}$	$1.5 \times 10^{-5}$	s
Packing density	$\rho_{pac}$	0.5	–
Effective layer thickness	$d_l$	100	$m \times 10^{-6}$

**Table 3** Material properties for Ti-6Al-4V and physical constants

Property	Symbol	Value	Unit	Source
Thermal diffusivity consolidated	$\alpha_c$	$5.66 \times 10^{-6}$	$m^2/s$	[43]
Thermal diffusivity powder	$\alpha_p$	$5.66 \times 10^{-7}$	$m^2/s$	[43, 44]
Specific heat capacity	$c_p$	771	J/kg K	[43]
Liquidus temperature	$T_{liq}$	1928	K	[53]
Density	$\rho$	4304	$kg/m^3$	[54]
Absorption coefficient	$\eta$	0.85	–	[42]
Emissivity powder	$\epsilon$	0.595	–	[55, 56]
Stefan-Boltzmann constant	$\sigma_{SB}$	$5.670 \times 10^{-8}$	$W/m^2K^4$	–
Universal gas constant	$R$	8.314	J/mol K	–
Activation energy of sintering	$Q$	$218 \times 10^3$	J/mol	[57]

**Acknowledgements** The authors gratefully acknowledge the HPC resources provided by the Erlangen National High Performance Computing Center (NHR@FAU) of the Friedrich-Alexander-Universität Erlangen-Nürnberg (FAU). Timo Berger is acknowledged for conducting the experimental reference process. The authors are grateful to Jakob Renner and Mohammad Reza Azadi Tinat for performing the beam measurement.

**Author Contributions** Conceptualisation, J.B., C.B. and C.K.; methodology, J.B., C.B., and C.K.; software, J.B. and C.B.; validation, J.B.; investigation, J.B.; resources, C.K.; data curation, J.B.; writing-original draft preparation, J.B.; writing-review and editing, J.B.; visualisation, J.B., M.M. and C.K.; supervision, M.M. and C.K.; project administration, M.M. and C.K.; funding acquisition, C.K. All authors have read and agreed to the published version of the manuscript.

**Funding** Open Access funding enabled and organized by Projekt DEAL. This project received funding from the European Research Council (ERC) under the European Union's Horizon 2020 research and innovation program (grant agreement No 101018634).

**Data Availability** Data supporting the findings of this study are available upon reasonable request from the corresponding author.

## Declarations

**Conflict of Interest** The authors declare no competing interests.

**Open Access** This article is licensed under a Creative Commons Attribution 4.0 International License, which permits use, sharing, adaptation, distribution and reproduction in any medium or format, as long as you give appropriate credit to the original author(s) and the source, provide a link to the Creative Commons licence, and indicate if changes were made. The images or other third party material in this article are included in the article's Creative Commons licence, unless indicated otherwise in a credit line to the material. If material is not included in the article's Creative Commons licence and your intended use is not permitted by statutory regulation or exceeds the permitted use, you will need to obtain permission directly from the copyright holder. To view a copy of this licence, visit <http://creativecommons.org/licenses/by/4.0/>.

## References

- Colosimo BM, Grasso M, Garghetti F, Rossi B (2022) Complex geometries in additive manufacturing: a new solution for lattice structure modeling and monitoring. *J Qual Technol* 54(4):392–414. <https://doi.org/10.1080/00224065.2021.1926377>
- Palmquist A, Jolic M, Hryha E, Shah FA (2023) Complex geometry and integrated macro-porosity: clinical applications of electron beam melting to fabricate bespoke bone-anchored implants. *Acta Biomater* 156:125–145. <https://doi.org/10.1016/j.actbio.2022.06.002>
- Raghavan N, Stump BC, Fernandez-Zelaia P, Kirka MM, Simunovic S (2021) Influence of geometry on columnar to equiaxed transition during electron beam powder bed fusion of In718. *Addit Manuf* 47:102209. <https://doi.org/10.1016/j.addma.2021.102209>
- Ramsperger M, Eichler S (2023) Electron beam based additive manufacturing of alloy 247 for turbine engine application: from research towards industrialization. *Metall Mater Trans A* 54(5):1730–1743. <https://doi.org/10.1007/s11661-022-06955-0>
- Reith M, Franke M, Körner C (2023) Impact of the acceleration voltage on the processing of  $\gamma$ -tial via electron beam powder bed fusion. *Prog Addit Manuf* 1–12. <https://doi.org/10.1007/s40964-023-00499-4>
- Körner C (2016) Additive manufacturing of metallic components by selective electron beam melting – a review. *Int Mater Rev* 61(5):361–377. <https://doi.org/10.1080/09506608.2016.1176289>
- Dang X, Li Y, Chen K, Ramamurthy U, Luo S, Liang X, He W (2022) Avoiding cracks in additively manufactured non-weldable directionally solidified ni-based superalloys. *Addit Manuf* 59:103095. <https://doi.org/10.1016/j.addma.2022.103095>
- Ramsperger M, Singer RF, Körner C (2016) Microstructure of the nickel-base superalloy CMSX-4 fabricated by selective electron beam melting. *Metall Mater Trans A* 47(3):1469–1480. <https://doi.org/10.1007/s11661-015-3300-y>
- Unocic KA, Kirka MM, Cakmak E, Greeley D, Okello AO, Dryepondt S (2020) Evaluation of additive electron beam melting of Haynes 282 alloy. *Mater Sci Eng A* 772:138607. <https://doi.org/10.1016/j.msea.2019.138607>
- Kirka MM, Fernandez-Zelaia P, Lee Y, Nandwana P, Yoder S, Acevedo O, Ryan D (2020) Mechanical performance of a non-weldable ni-base superalloy: Inconel 738 fabricated by electron beam melting. *Superalloys 2020*:1075–1084. [https://doi.org/10.1007/978-3-030-51834-9\\_105](https://doi.org/10.1007/978-3-030-51834-9_105)
- Biamino S, Penna A, Ackelid U, Sabbadini S, Tassa O, Fino P, Pavese M, Gennaro P, Badini C (2011) Electron beam melting of Ti-48Al-2Cr-2Nb alloy: microstructure and mechanical properties investigation. *Intermetallics* 19(6):776–781. <https://doi.org/10.1016/j.intermet.2010.11.017>
- Yang G, Yang P, Yang K, Liu N, Jia L, Wang J, Tang H (2019) Effect of processing parameters on the density, microstructure and strength of pure tungsten fabricated by selective electron beam melting. *Int J Refract Hard Met* 84:105040. <https://doi.org/10.1016/j.ijrmhm.2019.105040>
- Fernandez-Zelaia P, Ledford C, Ellis EAI, Campbell Q, Rossy AM, Leonard DN, Kirka MM (2021) Crystallographic texture evolution in electron beam melting additive manufacturing of pure molybdenum. *Mater Des* 207:109809. <https://doi.org/10.1016/j.matdes.2021.109809>
- Kaya D, Abdelmoula M, Küçüktürk G, Grossin D, Stamboulis A (2023) A novel approach for powder bed fusion of ceramics using two laser systems. *Materials* 16(6). <https://doi.org/10.3390/ma16062507>
- Heeling T, Gerstgrasser M, Wegener K (2017) Investigation of selective laser melting spatter characteristics for single- and multi-beam strategies using high speed imaging. *Lasers in Manufacturing Conference*
- Matthews MJ, Guss G, Drachenberg DR, Demuth JA, Heebner JE, Duoss EB, Kuntz JD, Spadaccini CM (2017) Diode-based additive manufacturing of metals using an optically-addressable light valve. *Opt Express* 25(10):11788–11800. <https://doi.org/10.1364/OE.25.011788>
- Fotovvati B, Shrestha S, Ferreri N, Duanmu N (eds) (2023) Experimental and Computational Study of Area Printing™ Additive Manufacturing: Inconel 718 and M300 Maraging Steel Density Improvement: University of Texas at Austin. <https://doi.org/10.26153/tsw/51013>
- Milberg J, Sigl M (2008) Electron beam sintering of metal powder. *Prod Eng* 2(2):117–122. <https://doi.org/10.1007/s11740-008-0088-2>
- Van DBJA, Hussey MJ, Richardson WT, Laidler I (2019) Improvements relating to additive layer manufacture using charged particle beams. US2019362936 (A1). RELIANCE PREC LIMITED
- Chiba A, Daino Y, Aoyagi K, Yamanaka K (2021) Smoke suppression in electron beam melting of Inconel 718 alloy powder based on insulator-metal transition of surface oxide film by mechan-

- ical stimulation. *Materials* 14(16):4662. <https://doi.org/10.3390/ma14164662>
21. Yim S, Bian H, Aoyagi K, Yanagihara K, Kitamura S-I, Manabe H, Daino Y, Hayasaka Y, Yamanaka K, Chiba A (2022) Ball-milling treatment of gas-atomized ti 48al 2cr 2nb powder and its effect on preventing smoking during electron beam powder bed fusion building process. *Addit Manufact* 51:102634. <https://doi.org/10.1016/j.addma.2022.102634>
  22. Yim S, Aoyagi K, Yanagihara K, Bian H, Chiba A (2023) Effect of mechanical ball milling on the electrical and powder bed properties of gas-atomized ti-48al-2cr-2nb and elucidation of the smoke mechanism in the powder bed fusion electron beam melting process. *J Mater Sci Technol* 137:36–55. <https://doi.org/10.1016/j.jmst.2022.07.024>
  23. Ackelid U (2021) Preheating of powder bed. SE2050445 (A1). FREEMELT AB
  24. Sjöström W, Koptyug A, Rännar L-E, Botero C (2024) Near-infrared radiation: a promising heating method for powder bed fusion. *Mater Manuf Process* 39(3):320–328. <https://doi.org/10.1080/10426914.2023.2195910>
  25. Larsson M, Snis A (2009) Method and device for producing three-dimensional objects. EP2049289 (A1). ARCAM AB
  26. Galati M, Iuliano L (2018) A literature review of powder-based electron beam melting focusing on numerical simulations. *Addit Manufact* 19:1–20. <https://doi.org/10.1016/j.addma.2017.11.001>
  27. Drescher P, Sarhan M, Seitz H (2016) An investigation of sintering parameters on titanium powder for electron beam melting processing optimization. *Materials* 9(12). <https://doi.org/10.3390/ma9120974>
  28. Shanbhag G, Vlasea M (2021) Effect of varying preheating temperatures in electron beam powder bed fusion: Part I Assessment of the effective powder cake thermal conductivity. <https://doi.org/10.48550/arXiv.2107.14684>. <http://arxiv.org/pdf/2107.14684.pdf>
  29. Liu Y, Yang Y, Mai S, Wang D, Song C (2015) Investigation into spatter behavior during selective laser melting of aisi 316l stainless steel powder. *Mater Des* 87:797–806. <https://doi.org/10.1016/j.matdes.2015.08.086>
  30. Young ZA, Guo Q, Parab ND, Zhao C, Qu M, Escano LI, Fezzaa K, Everhart W, Sun T, Chen L (2020) Types of spatter and their features and formation mechanisms in laser powder bed fusion additive manufacturing process. *Addit Manufact* 36:101438. <https://doi.org/10.1016/j.addma.2020.101438>
  31. Weiwei H, Wenpeng J, Haiyan L, Huiping T, Xinting K, Yu H (2011) Research on preheating of titanium alloy powder in electron beam melting technology. *Rare Met Mater Eng* 40(12):2072–2075. [https://doi.org/10.1016/S1875-5372\(12\)60014-9](https://doi.org/10.1016/S1875-5372(12)60014-9)
  32. Zäh M, Lutzmann S, Kahnert M, Walchshäusl F (2008) Determination of process parameters for electron beam sintering (ebs). In: Excerpt from the proceedings of the COMSOL conference Hannover
  33. Rausch AM, Küng VE, Pobel C, Markl M, Körner C (2017) Predictive simulation of process windows for powder bed fusion additive manufacturing: influence of the powder bulk density. *Materials* 10(10):1117. <https://doi.org/10.3390/ma10101117>
  34. Lin Z, Dadbakhsh S, Rashid A (2022) Developing processing windows for powder pre-heating in electron beam melting. *J Manuf Process* 83:180–191. <https://doi.org/10.1016/j.jmapro.2022.08.063>
  35. Yan W, Ma W, Shen Y (2020) Powder sintering mechanisms during the pre-heating procedure of electron beam additive manufacturing. *Mater Today Commun* 25:101579. <https://doi.org/10.1016/j.mtcomm.2020.101579>
  36. Rizza G, Galati M, Iuliano L (2022) A phase-field study of neck growth in electron beam powder bed fusion (eb-pbf) process of ti6al4v powders under different processing conditions. *Int J Adv Manuf Tech* 123(3–4):855–873. <https://doi.org/10.1007/s00170-022-10204-4>
  37. Rizza G, Galati M, Iuliano L (2022) Simulating the sintering of powder particles during the preheating step of electron beam melting process: review, challenges and a proposal. *Procedia CIRP* 112:388–393. <https://doi.org/10.1016/j.procir.2022.09.025>
  38. Wang Q, Zhang W, Li S, Tong M, Hou W, Wang H, Hao Y, Harrison NM, Yang R (2021) Material characterisation and computational thermal modelling of electron beam powder bed fusion additive manufacturing of ti2448 titanium alloy. *Materials* 14(23):7359. <https://doi.org/10.3390/ma14237359>
  39. Rahimi F, Pourabdollah P, Farhang Mehr F, Cockcroft S, Maijer D (2023) A macroscale heat transfer analysis of the build chamber in a commercial electron beam powder bed fusion (eb-pbf) additive manufacturing system during component fabrication. *Addit Manuf* 78:103831. <https://doi.org/10.1016/j.addma.2023.103831>
  40. Su H, Johnson DL (1996) Master sintering curve: a practical approach to sintering. *J Am Ceram Soc* 79(12):3211–3217. <https://doi.org/10.1111/j.1151-2916.1996.tb08097.x>
  41. Blaine DC, Park SJ, German RM, Suri P (2006) Application of work-of-sintering concepts in powder metals. *Metall Mater Trans A* 37(9):2827–2835. <https://doi.org/10.1007/BF02586115>
  42. Klassen A (2018) Simulation of evaporation phenomena in selective electron beam melting. FAU-Studien Materialwissenschaft und Werkstofftechnik, vol Band 19. FAU University Press, Erlangen. <https://open.fau.de/items/a75c9194-7039-4bdf-90af-a42519e1246e>
  43. Milošević N, Aleksić I (2012) Thermophysical properties of solid phase ti-6al-4v alloy over a wide temperature range. *Int J Mater Res* 103(6):707–714. <https://doi.org/10.3139/146.110678>
  44. Smith CJ, Tammam-Williams S, Hernandez-Nava E, Todd I (2017) Tailoring the thermal conductivity of the powder bed in electron beam melting (ebm) additive manufacturing. *Sci Rep* 7(1):10514. <https://doi.org/10.1038/s41598-017-11243-8>
  45. Kadioglu SY, Nourgaliev RR, Mousseau VA (2008) A comparative study of the harmonic and arithmetic averaging of diffusion coefficients for non-linear heat conduction problems. <https://doi.org/10.2172/928087>. <https://www.osti.gov/biblio/928087>
  46. Arnold C, Breuning C, Körner C (2021) Electron-optical in situ imaging for the assessment of accuracy in electron beam powder bed fusion. *Materials* 14(23) <https://doi.org/10.3390/ma14237240>
  47. Moin P (2012) Fundamentals of engineering numerical analysis, 2nd ed. edn. Cambridge University Press, Cambridge. <https://doi.org/10.1017/CBO9780511781438>
  48. Hunter JD (2007) Matplotlib: a 2d graphics environment. *Comput Sci Eng* 9(3):90–95. <https://doi.org/10.1109/MCSE.2007.55>
  49. Head T, Kumar M, Nahrstaedt H, Louppe G, Shcherbatyi I (2021) scikit-optimize/scikit-optimize. <https://doi.org/10.5281/zenodo.5565057>
  50. Mockus J (1982) The bayesian approach to global optimization. *Sys Mod Optim* 38:473–481. <https://doi.org/10.1007/BFb0006170>
  51. Shahriari B, Swersky K, Wang Z, Adams RP, Freitas N (2016) Taking the human out of the loop: a review of bayesian optimization. *Proc IEEE* 104(1):148–175. <https://doi.org/10.1109/JPROC.2015.2494218>
  52. Frazier P (2018) A tutorial on bayesian optimization. [arXiv.org. https://doi.org/10.48550/arXiv.1807.02811](https://doi.org/10.48550/arXiv.1807.02811)
  53. Boivineau M, Cagran C, Doytier D, Eyraud V, Nadal M-H, Wilthan B, Pottlacher G (2006) Thermophysical properties of solid and liquid ti-6al-4v (ta6v) alloy. *Int J Thermophys* 27(2):507–529. <https://doi.org/10.1007/PL00021868>
  54. Mills KC (2002) Recommended values of thermophysical properties for selected commercial alloys. Woodhead and ASM International, Cambridge and Materials Park op
  55. Hocine S, van Swygenhoven H, van Petegem S (2021) Verification

- of selective laser melting heat source models with operando x-ray diffraction data. *Addit Manuf* 37:101747. <https://doi.org/10.1016/j.addma.2020.101747>
56. Yang J, Sun S, Brandt M, Yan W (2010) Experimental investigation and 3d finite element prediction of the heat affected zone during laser assisted machining of ti6al4v alloy. *J Mater Process Technol* 210(15):2215–2222. <https://doi.org/10.1016/j.jmatprotec.2010.08.007>
57. Zallmann S, Fu Z, Körner C (2024) Powder sintering kinetics during electron beam based additive manufacturing. *Powder Technol* 434:119332. <https://doi.org/10.1016/j.powtec.2023.119332>

**Publisher's Note** Springer Nature remains neutral with regard to jurisdictional claims in published maps and institutional affiliations.